HHS Public Access

Author manuscript

Angiogenesis. Author manuscript; available in PMC 2015 March 31.

Published in final edited form as:

Angiogenesis. 2012 March ; 15(1): 87–98. doi:10.1007/s10456-011-9245-x.

In vivo laser speckle imaging reveals microvascular remodeling and hemodynamic changes during wound healing angiogenesis

Abhishek Rege,
Department of Biomedical Engineering, The Johns Hopkins University School of Medicine, Baltimore, MD, USA

Nitish V. Thakor,
Department of Biomedical Engineering, The Johns Hopkins University School of Medicine, Baltimore, MD, USA

Kevin Rhie, and
Russell H. Morgan Department of Radiology and Radiological Sciences, The Johns Hopkins University School of Medicine, 720 Rutland Ave, 217 Traylor Bldg, Baltimore, MD 21205, USA

Arvind P. Pathak
Russell H. Morgan Department of Radiology and Radiological Sciences, The Johns Hopkins University School of Medicine, 720 Rutland Ave, 217 Traylor Bldg, Baltimore, MD 21205, USA

Arvind P. Pathak: pathak@mri.jhu.edu

Abstract

Laser speckle contrast imaging (LSCI) is a high-resolution and high contrast optical imaging technique often used to characterize hemodynamic changes in short-term physiological experiments. In this study, we demonstrate the utility of LSCI for characterizing microvascular remodeling and hemodynamic changes during wound healing angiogenesis in vivo. A 2 mm diameter hole was made in the mouse ear and the periphery of the wound imaged in vivo using LSCI over 12 days. We were able to visualize and quantify the vascular and perfusion changes that accompanied wound healing in the microenvironment proximal to the wound, and validated these changes with histology. We found that consistent with the stages of wound healing, microvessel density increased during the initial inflammatory phase (i.e., day 0–3), stayed elevated through the tissue formation phase (i.e., until day 7) and returned to baseline during the tissue remodeling phase (i.e., by day 12). Concomitant ‘‘wide area mapping’’ of blood flow revealed that tissue perfusion in the wound periphery initially decreased, gradually increased from day 3–7, and subsided as healing completed. Interestingly, some regions exhibited a reestablishment of tissue perfusion approximately 6 days earlier than the ~ 18 days usually reported for the long term remodeling phase. The results from this study demonstrate that LSCI is an ideal platform for elucidating in vivo changes in microvascular hemodynamics and angiogenesis, and has the

---

© Springer Science+Business Media B.V. 2011

Correspondence to: Arvind P. Pathak, `pathak@mri.jhu.edu`.

Electronic supplementary material The online version of this article (doi:10.1007/s10456-011-9245-x) contains supplementary material, which is available to authorized users.

Author Manuscript Author Manuscript Author Manuscript Author Manuscript

Author Manuscript Author Manuscript Author Manuscript Author Manuscript

potential to offer invaluable insights in a range of disease models involving abnormal hemodynamics, such as diabetes and tumors.

Keywords

Angiogenesis; Hemodynamics; Laser speckle imaging; Wound healing; Vasculature

Introduction

Skin wounds elicit a natural healing response, whereby the body develops dermal and epidermal tissue to replace injured tissue. Mechanistically, the healing response has been divided into three overlapping phases—an inflammatory phase, a proliferative or new tissue formation phase and a tissue remodeling phase [1]. The immediate vascular response to wounding is that of clotting and vasoconstriction to minimize blood loss, but soon after, blood vessels dilate and become more permeable to allow elements of the immune system to access the wound site. This sequence of events constitutes the inflammatory phase. Beyond this initial response, tissue healing occurs concomitantly with robust neovascularization (i.e., the proliferative phase), which approximately starts on the second day and continues till epithelialization is complete. The vascular scar, caused by neovascularization, is eventually removed by apoptosis during the longer tissue remodeling phase. This study focuses on the in vivo characterization of vascular remodeling and angiogenesis that accompanies these phases of wound healing in a mouse ear wound model [2]. The mouse ear model is relevant to investigating disease states like sepsis [3] and diabetes [4] in which the wound healing mechanisms is impaired, and also to aging [5]. The cutaneous circulation of the murine ear model lends itself to optical imaging of blood vessel remodeling and hemodynamic changes without the technical challenges usually associated with in vivo imaging of traditional chamber [6] or subcutaneous models of wound healing [7].

While there have been several mechanistic studies on wound healing [8, 9], in vivo investigations of hemodynamic changes during the various wound healing phases have been limited. The skin circulation has been described as consisting of nutritive and arteriovenous perfusion [10]. The difference between them is that nutritive perfusion consists of blood flow through anastomotic vessels (capillaries) with multiple redundancies, while arteriovenous flow refers to well-regulated flow entering through arterioles and leaving through venules. In most wounds, blood flow has also been shown to re-distribute in collateral vessels when major vessels are injured [11]. Rendell et al. used Doppler flowmetry to demonstrate a rise and fall in blood flow during a 7 day long healing period in a rat dorsal skin wound model [12]. As this trend was observed for a region receiving nutritive perfusion from a vast network of capillaries, no observations were reported for functionally active regions receiving well-regulated perfusion from the arterioles.

In this paper, we demonstrate the utility of in vivo laser speckle contrast imaging (LSCI) for longitudinally monitoring spatio-temporal hemodynamic changes in a mouse ear model of wound healing. When tissue illuminated by a laser is photographed through a small aperture, the resulting images exhibit a random interference pattern, commonly called a *speckle*

Author Manuscript Author Manuscript Author Manuscript Author Manuscript

pattern. In tissue regions with blood vessels, this speckle pattern dynamically changes due to the continuous motion of red blood cells, causing a blur over the exposure time of the camera. The degree of blurring in the LSCI image is proportional to the velocity of blood in the vessels perfusing the region of interest (ROI) and constitutes the biophysical basis of LSCI. Therefore, LSCI can easily distinguish blood vessels from the relatively static background tissue without necessitating administration of an exogenous contrast agent. LSCI produces full field, high-resolution images of the microvasculature and the associated blood flow [13].

Traditionally, LSCI has been used for neurophysiological studies to dynamically image changes in cerebral blood flow [14, 15]. Recently there have also been reports describing the use of LSCI to study skin [16] and wound perfusion [17]. Here, for the first time, we elucidate in vivo changes in microvascular flow that accompany angiogenic changes in vascular architecture during the different phases of wound healing. LSCI is ideal for studying this phenomenon because without the introduction of any dyes, it can image blood vessels as small as 10–15 μm in diameter and the entire physiological range of blood flow velocities over a 6 mm × 6 mm field of view (FOV) without the need for raster scanning. These advantages made it possible to monitor both macro- and microvascular changes in regions proximal and distal to the wound site. The ability to assess angiogenesis induced vascular remodeling and perfusion trends over time have the potential to offer invaluable insights into therapeutic response and drug delivery in a range of disease models characterized by abnormal vasculature.

Materials and methods

While several animal models of wound healing exist [18], we chose the mouse ear model for this study because the ∼300 μm thick ear permits the microvasculature to be clearly visualized using optical techniques such as LSCI. Additionally, to avoid autofluorescence from the mouse fur we used hairless, immunocompetent SKH1 mice for this study.

Animal preparation and wounding

All animal procedures were performed in accordance with protocols approved by the Johns Hopkins Animal Care and Use Committee. Eleven 8–12 week old male SKH1 mice were anesthetized with intraperitoneal administration of 0.15 ml of a mixture of ketamine (50 mg/kg) and xylazine (5 mg/kg). An ear wound was created by punching a 2 mm diameter circular hole (full thickness) in the center of the right ear (pinna) using a biopsy punch. While some studies create an injury only as deep as the cartilage layer [19], we created a full thickness wound or through hole, to ensure reproducibility of the wound and stability of the injury. The wound was disinfected with ethanol swabs to prevent infection. Then, the mouse ear was gently restrained between a glass slide (bottom) and a cover slip (top) separated by 300 μm spacers. A 50 mg weight was added to the spacers to keep the pinna flattened during LSCI imaging. This set up was only employed during imaging and allowed us to restrain the ear without occluding any microvessels, while maintaining a constant pressure on the ear during each imaging session. The body temperature of each mouse was measured before and after each imaging session using a rectal thermometer.

Author Manuscript

Author Manuscript

Author Manuscript

Author Manuscript

LSCI setup and imaging protocol

A 12-bit cooled CCD camera (PCO, Kelheim, Germany) was used to acquire a sequential stack of 80 raw speckle images of the mouse ear under red (632 nm) laser illumination (JDSU, Milpitas, CA), as shown in Fig. 1a. The magnification was set to 1:1 and the aperture set to an *f*-number of 4.0 using a 60 mm, *f*/2.8 macro lens mounted on the camera. The images were acquired at 10 frames/s with the camera exposure time set to 16 ms. The speckle images witness blurring over the exposure time of the camera, which is more pronounced in vascularized regions on account of the motion of red blood cells. Mathematically, this blur can be quantified in terms of the laser speckle contrast (K), which is calculated for every pixel (x, y) in the time domain using Eq. 1.

$$K(x,y)=\frac{\sigma_{80}(x,y)}{\mu_{80}(x,y)} \quad (1)$$

where, μ_{80} and σ_{80} are the mean intensity and standard deviation of each pixel (x, y) computed from the series of 80 images. Plotting the speckle contrast values produced high spatial resolution, high contrast LSCI images of the mouse ear microvasculature (Fig. 1b). Blood flow was also inferred from the speckle contrast values as follows: it is known that the velocity of blood flow is inversely related to the correlation time (τ_c) of speckle fluctuations [20], which can be calculated from the laser speckle contrast values using Eq. 2 [21, 22].

$$K^2=\frac{\tau_c}{2T}\left[2-\frac{\tau_c}{2T}\left\{1-\exp\left(-\frac{2T}{\tau_c}\right)\right\}\right] \quad (2)$$

Here $1/\tau_c$ provides an estimate of the blood flow velocity, T is the exposure time of the camera and K the laser speckle contrast is calculated using Eq. 1. Accordingly, $1/\tau_c$ values were calculated for every pixel and plotted in pseudo-color to illustrate estimates of blood flow in the wound periphery. Since blood flow velocity and perfusion are related via the vessel diameter, in this study, maps of $1/\tau_c$ are referred to as estimates of tissue blood flow or perfusion. The reader is referred to [23] for a more detailed analysis of the flow—velocity—$1/\tau_c$ relationship. In addition, a white light reflectance image of the mouse ear was routinely taken for comparison. After the day of wound creation (day 0), mice ears were imaged using the same procedure on days 3, 5, 7, 10 and 12. Between imaging days, the mice were housed in the animal facility.

Post-processing of LSCI images

All post-processing was done using MATLA® (Math-works, MA). Since our goal was to use sequential LSCI to longitudinally track hemodynamic changes in the mouse ear vasculature over multiple days, we processed images to account for day-to-day variations in orientation of the mouse ear with respect to both, illumination and camera placement. The sequence of post-processing steps is summarized in Fig. 1c.

Registration of the LSCI image series—We used a manually supervised, semi-automatic scheme to register all subsequent images to images acquired on day 0. By

Author Manuscript

Author Manuscript

Author Manuscript

Author Manuscript

manually specifying 6–8 seed pixels for each vessel image, an initial ‘‘coarse’’ registration was implemented using an affine transformation [24]. Final registration was achieved by minimizing the pixel-wise cross-correlation coefficient between every pair of images within a user-defined square ROI. The square ROI was chosen such that it included the edges of a major vessel distal to the wound. Following registration, the FOV was cropped and smoothed using a 3 × 3 pixel median filter to remove single pixel noise.

Normalization of LSCI image intensity—Signal intensity normalization was necessary to correct for two causes of LSCI image intensity variations. First, the Gaussian profile of the illuminating laser beam produces a non-uniformly illuminated FOV. We corrected for this using a previously reported scheme [25] in which we employ a Gaussian model to approximate the signal intensity of the pixel depending on its spatial location within the FOV. Second, to enable comparison of hemodynamic changes between different days of imaging, the signal intensity of each image was normalized to the intensity of the background tissue in the ear periphery, distal to the wound site. The background intensity was defined as the 95th percentile of the signal intensity histogram of the LSCI image under consideration. Following normalization, the intensity of each grayscale LSCI image ranged from 0 to 1. This normalization approach assumes that the perfusion of background ROIs distal to the wound remains unchanged between imaging sessions. To make the visualization of hemodynamic changes more intuitive, $1/\tau_c$ maps were computed from normalized LSCI images and displayed in pseudo color. High blood flows were represented by hot (red) colors while lower blood flows were represented by cool (blue) colors in the $1/\tau_c$ maps.

LSCI image analyses

Vascular morphology metrics—To elucidate angiogenesis induced changes in vascularization, blood vessels were manually segmented from LSCI images for each mouse and at every time point to obtain a binary image of the vasculature. These binarized blood vessels were skeletonized (i.e., reduced to a single pixel thin trace), so that vessel length could be calculated. The length of these skeletonized vessels was then calculated at each time point to quantify changes in the vascular structure that occurred during the healing process. In addition to vessel length, a metric was needed that was sensitive to small length microvessels that are typical of angiogenic microenvironments, rather than longer parent vessels that are also known to become more tortuous during angiogenesis. Consequently, we counted the number of terminal vessel branches (*terminal branch count, or TB count*) as an index of neovascularization. The TB count was estimated by counting the endpoints of vessel centerlines in the binarized vascular traces. Subsequently, the overall spatial densities of both vessel length and TB counts were calculated by dividing each by the total area of healing skin. This area was calculated by subtracting the area of the circular wound from that of the ROI. Finally, tortuosity of parent vessels was calculated to determine the morphological changes in the parent macrovessel feeding the wounded region. To do this, the vein closest to the wound margin that drains blood away from the ear was manually traced along its entire length. At branch points, the largest branch closest to the wound was followed. A single pixel thin centerline was obtained for the vessel trace using the binary ‘skeletonization’ operator in MATLAB. Subsequently tortuosity of this centerline was

Author Manuscript

calculated based on the number of times its curvature changes along the length of the vessel [26, 27], and was calculated as follows:

$$T=\int_{x_1}^{x_2}\frac{(\kappa'(x))^2dx}{L} \quad (3)$$

$$\kappa=\frac{(f''(x))}{(1+(f'(x))^2} \quad (4)$$

where L is the length of the vessel, x is a parametric variable along the straight line between vessel end points x_1 and x_2, $f(x)$ is the function describing the vessel pixel location, $f'(x)$ and $f''(x)$ are first and second derivatives of $f(x)$ respectively, k is the curvature of $f(x)$, and T is the tortuosity of the vessel. The tortuosity was also normalized to its value on day 0 to elucidate its trend through the healing period.

Analyses of spatiotemporal changes in blood flow—To assess spatio-temporal changes in hemodynamics at the wound periphery, blood flow data (i.e., $1/\tau_c$ values calculated using Eq. 2) from all mice in the experimental group for each time point were averaged in every annular sector and visualized as a circular plot for that time point. On this plot, the wound was represented as a central circle of fixed diameter, and every 50 μm wide annulus around the wound was represented as a concentric ring. In other words, radial distance on each plot represented the shortest distance of the region from the wound outline. Similarly, the angle ($0° < \theta < 360°$) on the plots was the angle that a line joining the region with the wound center subtended with the line joining the base of the ear with wound center in the counter clockwise direction.

Immunofluorescence microscopy protocol—Adjacent 10 μm frozen ear sections were cut onto silanized glass slides and vascular basement membrane immunostained using an anti-mouse laminin primary antibody (Sigma, St. Louis, MO) and anti-rabbit AlexaFluor 488 secondary antibody (Invitrogen, Carlsbad, CA). Slides were counterstained with DAPI and cover-slipped. Laminin staining was chosen in our experiment as it plays an important role in angiogenesis and has been employed as an immunohistochemical marker of the angiogenic vasculature [28–30]. Counterstaining with DAPI made the nuclei of the granulation tissue visible. Slides were imaged on a Nikon ECLIPSE-TS100 microscope (Nikon Instruments Inc., Melville, NY) with the appropriate filters for detecting immunofluorescence. ROIs were digitized at 2× and 40 × magnification using a SPOT INSIGHT™ CCD camera (Diagnostic Instruments Inc., Sterling Heights, MI). Care was taken to ensure that ROIs acquired for image analysis excluded autofluorescent cutaneous structures such as hair follicles and sebaceous glands. The fractional area of the laminin staining was quantified within each ROI using a customized macro written for ImageJ (Rasband WS, ImageJ, National Institutes of Health, Bethesda, MD, USA, http://imagej.nih.gov/ij/). Briefly, the intensity of the each mouse ear image was normalized to cover the entire intensity range (0–1). Thereafter, background fluorescence was eliminated using a *rolling ball* algorithm following which, laminin-positive structures were identified using *k-means* clustering. A three-group clustering procedure was performed and the

Author Manuscript

Author Manuscript

Author Manuscript

Author Manuscript

resulting image thresholded based on results of clustering: one cluster identified the tissue background, while the other two clusters identified laminin-positive structures. Next, the resulting binary image was morphologically processed using a *binary connectivity* filter to retain vessel-like features while rejecting unconnected features, such as isolated pixels. Finally, the fractional area was calculated as the fraction of pixels remaining as a percentage of the total number of pixels in the ROI.

Statistics—Wound healing experiments were performed in eleven mice. Two mice were sacrificed on each of days 3, 5 and 7 and the remaining mice were sacrificed on day 12 for histology. Thus, our sample sizes for each time was point as follows: N_{day0} =11, N_{day3} =11, N_{day5} = 9, N_{day7} = 7, N_{day10} = 5 and $N_{\text{day}}12$ = 5. A two-tailed, nonparametric Mann–Whitney U-test was used ($\alpha = 0.05$) to determine whether median hemodynamic, morphologic and histological parameters were significantly different between subsequent time points.

Results

We imaged 12 mice, of which 11 were wounded on day 0 and one unwounded mouse served as a control. One of the wounded mice sustained a secondary injury and was excluded from subsequent analyses. Two mice were sacrificed on days 3, 5 and 7, and the remaining four sacrificed on day 12 for post mortem analysis of the microvas culature in the wound periphery. Every mouse was imaged using LSCI until the day of sacrifice.

LSCI can longitudinally track angiogenic changes in vivo during wound healing

LSCI was capable of simultaneously monitoring changes in the microvascular architecture and hemodynamics over the entire course of wound healing. Figure 2a–f shows sequential LSCI images of the wound periphery on days 0, 3, 5, 7, 10 and 12, respectively. The increase in neovascularization (Fig. 2g–l) and the redistribution of blood flow (Fig. 2m–r) are clearly visible in these images. The second column (Fig. 2g–l) clearly demonstrates the sensitivity of LSCI to angiogenesis occurring on days 3, 5 and 7. These angiogenic changes are not visible in either day 0 (Fig. 2a, g, m) or control images (Fig. 2s–x). The third and fourth columns (Fig. 2m–x) show LSCI images in which $1/\tau_c$ values are displayed in pseudo-color to indicate the relative blood flow through each vessel segment. These images unequivocally demonstrate the ability of LSCI to extract and quantify useful information associated with the in vivo angiogenic microenvironment.

LSCI can characterize in vivo changes in vascular morphology that accompany wound healing

Figure 3a shows that the vessel length density (per unit area) increased significantly from day 0 (2.11 ± 0.17 mm^{-1}) to day 3(2.55 ± 0.20 mm^{-1}) that is, by a factor of 1.24 ± 0.09 (P = 0.02) and remained elevated from day 3 to day 7, relative to day 0. On days 10 and 12, the vessel length density was observed to be lower than that for day 7 suggesting a return toward baseline. In control animals, the vessel length density relative to day 0 was 1.022 ± 0.021. The TB count density showed a similar trend as it increased from day 0 to day 3 by a factor of 1.29 ± 0.09 (P = 0.01), remained elevated until day 7 and subsequently decreased.

Author Manuscript

Author Manuscript

Author Manuscript

Author Manuscript

The TB count density in control animals relative to day 0 was 1.033 ± 0.017, which was 25% lower than in healing animals. The vessel length and TB densities measured on days 10 and 12 were not significantly different from day 0 values ($P = 0.93$ and $P = 0.90$, respectively).

Angiogenesis induces changes in vascular tortuosity of parent vessels during wound healing

Figure 3b illustrates changes in tortuosity (calculated using Eqs. 3 and 4) of the closest parent vessel feeding the wound during the course of wound healing. In controls, vessel tortuosity remained constant relative to day 0 at 1.001 ± 0.001. In the wounded animals, the vessel tortuosity increased from baseline (day 0) to 4.14 ± 1.10 on day 3, with a maximum of 8.07 ± 3.44 on day 5. The tortuosity eventually decreased but remained higher than baseline tortuosity, as indicated by the day 12 value of 2.73±0.79. Additionally, the tortuosity of the vasculature in the wounded ear stayed elevated relative to that in the control ear throughout the entire healing period.

In vivo changes in microvascular blood flow in the wound periphery

Figure 4 illustrates the mean blood flow (averaged in every annular sector over all mice in the cohort) in the wound periphery as a function of its radial orientation (radius and angle) with respect to the base of the ear. It was possible to construct this circular plot because the standard error for each annular sector was low (mean = 10% and median = 8%). Note that the wound on day 0 had a diameter of 2 mm that decreased in size due to wound contraction on subsequent days. Salient observations were made in the following regions of interest—*wound (W), proximal region (P), upstream region (U) and two downstream regions* (D1 and D2). The mean blood flow in region U was 0.25 (arbitrary units) over the six imaging sessions and changed slightly over the course of healing as suggested by the low standard error of 0.02. Parts of region D1 witnessed a sharp decrease in blood flow on day 0 after the ear was wounded as suggested by a mean blood flow of 0.067 ± 0.004, which was lower than the blood flow in the same region in the control ear (0.216 ± 0.002). Region D2 witnessed a significant increase in blood flow from day 0 (0.25 ± 0.01) to day 5 (0.42 ± 0.02) after which, the flow returned to baseline (control) levels. Region D1 exhibited a similar trend, but the peak blood flow was lower than that in D2. The blood flow in the region proximal to the wound (P) stayed lower than for other regions throughout the healing period and slowly returned to baseline by day 12. Note that some sectors distal to the wound on days 5 and 7 were not plotted because these regions partly lay outside the FOV in some mice.

Histological changes in vascularization in the wound periphery

Figure 5 summarizes the results of histological findings over the entire course of wound healing. Figure 5a – h shows low (2×) and high (40×) magnification images of the vascularization in the wound periphery. Labeling the vascular basement membrane with an antibody against laminin (Supplementary Fig. S1–S2) confirmed the occurrence of sprouting angiogenesis during the proliferative phase of wound healing and the gradual revascularization of the granulation tissue (Fig. 5e – h) initially assessed with LSCI. Figure

Author Manuscript Author Manuscript Author Manuscript Author Manuscript

5i shows that the fractional area of laminin staining was significantly elevated at days 5 and 12 relative to day 3 (*P* = 0.03 and *P* = 0.002, respectively), while that on days 5 and 12 was significantly greater than day 7 (*P* = 0.02 and *P* = 0.002, respectively).

Discussion

LSCI can longitudinally track angiogenic changes in vivo during wound healing

In murine models of wound healing, only those models which naturally limit wound contraction, such as the ear of the hairless mouse, have utility for analysis of wound healing angiogenesis and hemodynamics [19, 31]. Since the total thickness of the hairless mouse ear is approximately 300 lm and nutrients are supplied by three to four primary vascular clusters that enter the ear at the base and fan out towards the periphery, this model lends itself extremely well to an in vivo LSCI study of wound healing [19]. The combination of LSCI and the mouse ear model also enabled us to circumvent the technical difficulties associated with chamber models of wound healing [6]. For example, the relatively simpler ear wound preparation makes it more amenable to repeatable and robust optical imaging with LSCI. Here, we demonstrate the utility of LSCI as a powerful new platform for characterizing in vivo microvascular remodeling and hemodynamic changes that accompany wound healing angiogenesis.

Recently other optical techniques such as intravital microscopy [32], photoacoustic tomography [33] and optical frequency domain imaging [34] have been employed to probe the angiogenic microenvironment in vivo. However, the relatively simple and inexpensive in vivo LSCI approach achieves the ideal combination of imaging at the micro- and macroscopic spatial scales. This permits ‘‘wide area mapping’’ or imaging of the entire vascular network at high spatial resolution along with the quantification of a range of microvascular parameters. For example, LSCI can quantify changes in microvessel architecture that accompany angiogenesis while simultaneously providing macrovascular information such as vessel tortuosity, and functional information such as blood flow. This bestows LSCI with an inherent advantage over high magnification microscopy techniques such as optical coherence tomography (OCT), which provide high spatial resolution at the expense of FOV coverage [35]. LSCI is also more suitable than techniques such as Doppler flowmetry for assessing ‘‘microvascular’’ hemodynamics because the latter while capable of measuring regional changes in blood flow at spatial resolutions >100 μm, does not provide any information regarding the microvascular architecture [36]. This is especially crucial when one is interested in assessing microvascular changes during the initial stages of angiogenesis. Furthermore, the straightforward instrumentation of LSCI permits it to be used in combination with other techniques such as optical spectroscopy for extracting physiological parameters such as tissue oxygenation [37].

LSCI can characterize in vivo changes in vascular morphology that accompany wound healing

LSCI permitted the characterization of in vivo changes in vascular morphology during the different stages of wound healing. The vascular morphology metrics (vessel length and terminal branch count) exhibited a similar trend (Fig. 3a); namely, a significant increase

Author Manuscript Author Manuscript Author Manuscript Author Manuscript

during the inflammatory phase (i.e., days 0–3), elevated values from during the new tissue formation phase (i.e., days 3–7) followed by an eventual return towards baseline during the tissue remodeling phase (i.e., days 10–12). The histological results provided independent validation of this trend. These observations are consistent with the angiogenic response during the three major phases of wound healing observed by other investigators [6, 19]. For example, immediately following the injury, the ‘‘inflammatory’’ phase of wound healing ensures that inflammatory cells flock to the wound site to prevent infection. These inflammatory cells also secrete a slew of growth/angiogenic factors [38] necessary for new or granulation tissue formation phase and the recruitment of endothelial cells to the wound site. During the granulation tissue formation phase, activated endothelial cells participate in blood vessel sprouting at the wound edge and a new vasculature begins to develop [39]. Finally, during the tissue remodeling phase the transformation of granulation tissue into scar tissue is characterized by the regression of microvessels through apoptosis of endothelial cells and the differentiation of newly formed blood vessels into mature vascular structures. Our observations are consistent with these wound healing dynamics. It should be borne in mind that because the speckle signal is derived from the movement of erythrocytes inside blood vessels, LSCI can only image perfused or patent blood vessels. Therefore, the increase and decrease in vessel length and TB count should be interpreted as changes in the architecture of perfused microvessels. The return to baseline of vessel length and TB densities suggests the perfusion in the murine ear reverts to an optimal blood supply via neovessels and redundancies in the microvasculature, following wound healing. Our data also suggests that cutaneous tissue undergoing healing can witness restoration of blood flow to pre-wound baseline values earlier (∼day 12) than the ∼18 days reported for the long term remodeling phase [40, 41].

Angiogenesis induced changes in vascular tortuosity of parent vessels during wound healing

In this study we also observed a change in the vascular tortuosity of parent blood vessels during wound healing (Fig. 3b). Vessel tortuosity eventually decreased on days 10 and 12 but remained above baseline values. As mentioned above, angiogenesis is initiated by endothelial cells migrating and proliferating in the wound site and is maintained as long as necessary by various angiogenic factors. Therefore, the elevated tortuosity of the parent vessels may be attributable to the sustained release of proangiogenic growth factors such as VEGFA during the remodeling phase of wound healing [42].

In vivo changes in microvascular blood flow in the wound periphery

A unique aspect of this study was our ability to characterize in vivo changes in microvascular perfusion in the wound periphery using LSCI. Spatio-temporal analysis of tissue blood flow provided insight into the evolution of hemodynamic changes in different regions in the wound periphery. For example, the initial dip in blood flow within region D1 (Fig. 4) distal to the wound can be attributed to the loss of perfusion or hemostasis due to wounding. The low blood pressure in downstream vessels probably precludes the immediate recovery of perfusion in this region via collaterals. This is to be expected, as the blood flow upstream of the wound was not affected due to the presence of redundancies in the circulation that even shunted blood away from injured vessels. The differences in blood flow

Author Manuscript

Author Manuscript

Author Manuscript

Author Manuscript

witnessed by the two regions D1 and D2 (Fig. 4) downstream of the wound is likely attributable to the location of the injury. The wound was created to the left of a major vessel (Fig. 4); consequently the proximal region (P) received its blood supply from region D2, instead of D1. The LSCI measurements in region P are consistent with blood flow changes expected in angiogenic vessels, i.e., an increase in blood volume, robust sprouting of neovasculature accompanied by a marginal increase in blood flow velocities. This phenomenon can be appreciated intuitively if one considers that angiogenic remodeling involves the sprouting of capillary-sized vessels from mother vessels with low blood velocities, often venules [43]. The initial hemostasis followed by the recovery of blood flow within 3–5 days mediated by angiogenesis, and growth of collaterals are all consistent with our current understanding of the positive and negative regulation of angiogenesis during the different phases of wound healing [42]. This view is further bolstered by the concomitant changes in terminal branch density that we also measured over the same period.

Histological changes in vascularization in the wound periphery

Immunofluorescent labeling of mouse ear tissue sections served the dual purpose of validating our LSCI based findings as well as independently characterizing overall changes in vascularization during wound healing. In the region proximal to the wound, the increase and decrease in fractional area of laminin from day 0 to 7 suggests the establishment and stabilization of the neovasculature that accompanies epithelization [44]. The high fractional area of laminin on day 12 suggests continued establishment of the vascularization as the wound contracts [44]. However, the trend in laminin staining did not fully mimic the trends in vessel length and terminal branch count measured in vivo with LSCI. This is probably attributable to variations in the histologic data resulting from the limited number of ROIs that could be imaged. It is also possible that in spite of our best efforts, some of the analyzed ROIs included contributions from autofluorescent cutaneous structures

The ability to simultaneously quantify the spatial and temporal evolution of vascular remodeling and blood flow in vivo can be used to investigate abnormalities in different phases of wound healing, better understand the physiological basis of angiogenesis and approaches to modulate it, and to test novel therapeutics. Our results suggest a characteristic spatial distribution and evolution of perfusion changes that may be exploited to influence local or topical delivery strategies of therapeutic agents such insulin or silver nanoparticles [45, 46], and help understand the regional biodistribution of systemically administered drugs. In vivo LSCI-based flow and vascularization metrics could also provide a non-invasive indication of the degree of wound healing. For example, LSCI could find use in measuring the efficiency of novel therapies that promote wound healing, which is known to be impaired in diabetic patients [47, 48]. Harold Dvorak’s classic postulation that ‘‘tumors are wounds that do not heal’’ [49] suggests that key molecular mechanisms in wound healing may also offer strategic insights for managing pathological angiogenesis in cancer. Therefore, the murine ear wound healing model may serve as an ideal surrogate model for understanding the fundamental aspects of the tumor microenvironment, such as modulation of the blood flow distribution by angiogenesis. More recently, vascular normalization has been proposed as a new paradigm for effective anti-tumor therapy since the haphazard tumor blood flow drastically impedes drug delivery to tumors [50]. The restoration of tissue

Author Manuscript Author Manuscript Author Manuscript Author Manuscript

perfusion even before restoration of vessel architecture, as we observed in the mouse ear wound healing model, could offer new insights into this concept. Finally, it is possible that both individually and collectively, the parameters assessed in this study could have prognostic value for assessing the in vivo status of the wound microenvironment. For example, vessel tortuosity, which has been known to increase during angiogenesis [51], has been shown to be an independent indicator of brain tumor malignancy [52], and a similar approach could be investigated for wound healing.

Conclusions

LSCI is a high-resolution and high contrast in vivo optical technique that does not require the administration of contrast agents and thus, is an excellent platform for studying the microcirculation. In this paper, we successfully demonstrated the suitability of LSCI for characterizing the microvascular remodeling and hemodynamic changes that accompany wound healing angiogenesis. Both new vessel length and parent vessel tortuosity were observed to increase in the wound periphery until day 7 after which each decreased towards their respective baseline value, a finding corroborated by histology. We demonstrated LSCI's capability to create ''wide area'' maps of the entire wound periphery, including spatio-temporal information about micro- and macro-vascular morphology and perfusion. We believe that LSCI is ideally suited to elucidating in vivo changes in microvascular hemodynamics and angiogenesis in a range of disease models involving abnormal hemodynamics, such as diabetes and tumors.

Supplementary Material

Refer to Web version on PubMed Central for supplementary material.

Acknowledgments

This work was supported jointly by National Institute of Aging award number R01AG029681, Department of Health and Human Services award number 1R43CA139983-01, and a JHU Institute of NanoBiotechnology (INBT) Junior Faculty Pilot Award. We gratefully acknowledge Peng Miao for assistance with image registration.

References

1. Singer AJ, Clark RAF. Cutaneous wound healing. New Eng J Med. 1999; 341:738–746. [PubMed: 10471461]
2. Kiyama T, Naito M, Shitama H, Shinoda T, Maeyama A. Comparison of skin blood flow between mini- and standard-incision approaches during total hip arthroplasty. J Arthroplast. 2008; 23:1045–1049.
3. Koskela M, Gaddnas F, Ala-Kokko TI, Laurila JJ, Saarnio J, et al. Epidermal wound healing in severe sepsis and septic shock in humans. Crit Care. 2009; 13:R100. [PubMed: 19552820]
4. Ngo BT, Hayes KD, DiMiao DJ, Srinivasan SK, Huerter CJ, et al. Manifestations of cutaneous diabetic microangiopathy. Am J Clin Dermatol. 2005; 6:225–237. [PubMed: 16060710]
5. Chung JH, Eun HC. Angiogenesis in skin aging and photoaging. J Dermatol. 2007; 34:593–600. [PubMed: 17727362]
6. Sorg H, Krueger C, Vollmar B. Intravital insights in skin wound healing using the mouse dorsal skin fold chamber. J Anat. 2007; 211:810–818. [PubMed: 18005122]
7. Demirdogen B, Elcin AE, Elcin YM. Neovascularization by bFGF releasing hyaluronic acid-gelatin microspheres: in vitro and in vivo studies. Growth Factors. 2010; 28:426–436. [PubMed: 20854186]

Author Manuscript

Author Manuscript

Author Manuscript

Author Manuscript

8. Rendell MS, Johnson ML, Smith D, Finney D, Capp C, et al. Skin blood flow response in the rat model of wound healing: expression of vasoactive factors. J Surg Res. 2002; 107:18–26. [PubMed: 12384060]
9. Shaterian A, Borboa A, Sawada R, Costantini T, Potenza B, et al. Real-time analysis of the kinetics of angiogenesis and vascular permeability in an animal model of wound healing. Burns. 2009; 35:811–817. [PubMed: 19423227]
10. Rendell MS, Milliken BK, Finnegan MF, Finney DE, Healy JC, et al. The microvascular composition of the healing wound compared at skin sites with nutritive versus arteriovenous perfusion. J Surg Res. 1998; 80:373–379. [PubMed: 9878340]
11. North KA, Sanders AG. The development of collateral circulation in the mouse's ear. Circ Res. 1958; 6:721–727. [PubMed: 13585598]
12. Rendell MS, Milliken BK, Finnegan MF, Finney DA, Healy JC. The skin blood flow response in wound healing. Microvasc Res. 1997; 53:222–234. [PubMed: 9211400]
13. Murari K, Li N, Rege A, Jia X, All A, et al. Contrast-enhanced imaging of cerebral vasculature with laser speckle. Appl Opt. 2007; 46:5340–5346. [PubMed: 17676149]
14. Dunn AK, Bolay H, Moskowitz MA, Boas DA. Dynamic imaging of cerebral blood flow using laser speckle. J Cereb Blood Flow Metab. 2001; 21:195–201. [PubMed: 11295873]
15. Ayata C, Dunn AK, Gursoy OY, Huang Z, Boas DA, et al. Laser speckle flowmetry for the study of cerebrovascular physiology in normal and ischemic mouse cortex. J Cereb Blood Flow Metab. 2004; 24:744–755. [PubMed: 15241182]
16. Nakagami G, Sari Y, Nagase T, Iizaka S, Ohta Y, et al. Evaluation of the usefulness of skin blood flow measurements by laser speckle flowgraphy in pressure-induced ischemic wounds in rats. Ann Plast Surg. 2010; 64:351–354. [PubMed: 20179489]
17. Stewart CJ, Gallant-Behm CL, Forrester K, Tulip J, Hart DA, et al. Kinetics of blood flow during healing of excisional full-thickness skin wounds in pigs as monitored by laser speckle perfusion imaging. Skin Res Technol. 2006; 12:247–253. [PubMed: 17026655]
18. Davidson JM. Animal models for wound repair. Arch Dermatol Res. 1998; 290(Suppl):S1–S11. [PubMed: 9710378]
19. Barker JH, Kjolseth D, Kim M, Frank J, Bondar I, et al. The hairless mouse ear: an in vivo model for studying wound neovascularization. Wound Repair Regen. 1994; 2:138–143. [PubMed: 17134383]
20. Ramirez-San-Juan JC, Ramos-García R, Guizar-Iturbide I, Martínez-Niconoff G, Choi B. Impact of velocity distribution assumption on simplified laser speckle imaging equation. Opt Express. 2008; 16:3197–3203. [PubMed: 18542407]
21. Bandyopadhyay R, Gittings A, Suh S, Dixon P, Durian D. Speckle-visibility spectroscopy: a tool to study time-varying dynamics. Rev Sci Instrum. 2005; 76:0931101–0931111.
22. Duncan DD, Kirkpatrick SJ. Can laser speckle flowmetry be made a quantitative tool? J Opt Soc Am A Opt Image Sci Vis. 2008; 25:2088–2094. [PubMed: 18677371]
23. Rege, A.; Murari, K.; Li, N.; Thakor, NV. Imaging microvascular flow characteristics using laser speckle contrast imaging; Buenos Aires. Proc 32nd Ann Intl Conf IEEE Engr Med Biol Soc; 2010. p. 1978-1981.http://www.ncbi.nlm.nih.gov/pubmed/21096787
24. Barber DC. Registration of low resolution medical images. Phys Med Biol. 1992; 37:1485–1498. [PubMed: 1631194]
25. Miao, P.; Li, N.; Rege, A.; Tong, S.; Thakor, NV. Model based reconstruction for simultaneously imaging cerebral blood flow and deoxyhemoglobin distribution; Minneapolis. Proc 31st Ann Intl Conf IEEE Engr Med Biol Soc; 2009. p. 3236-3293.http://www.ncbi.nlm.nih.gov/pubmed/19964288
26. Patasius, M.; Marozas, V.; Lukosevicius, A.; Jegelevicius, D. Model based investigation of retinal vessel tortuosity as a function of blood pressure: preliminary results; Lyon. Proc 29th Ann Intl Conf IEEE Engr Med Biol Soc; 2007. p. 6459-6462.http://www.ncbi.nlm.nih.gov/pubmed/18003504
27. Hart WE, Goldbaum M, Côté B, Kube P, Nelson MR. Measurement and classification of retinal vascular tortuosity. Int J Med Inform. 1999; 53:239–252. [PubMed: 10193892]

Author Manuscript

Author Manuscript

Author Manuscript

Author Manuscript

28. Davis GE, Senger DR. Endothelial extracellular matrix: biosynthesis, remodeling, and functions during vascular morphogenesis and neovessel stabilization. Circ Res. 2005; 97:1093–1107. [PubMed: 16306453]
29. Simon-Assmann P, Orend G, Mammadova-Bach E, Spenle C, Lefebvre O. Role of laminins in physiological and pathological angiogenesis. Int J Dev Biol. 2011; 55:455–465. [PubMed: 21858771]
30. Pettersson A, Nagy JA, Brown LF, Sundberg C, Morgan E, et al. Heterogeneity of the angiogenic response induced in different normal adult tissues by vascular permeability factor/ vascular endothelial growth factor. Lab Invest. 2000; 80:99–115. [PubMed: 10653008]
31. Bondar I, Uhl E, Barker JH, Galla TJ, Hammersen F, et al. A new model for studying microcirculatory changes during dermal wound healing. Res Exp Med (Berl). 1991; 191:379–388. [PubMed: 1775730]
32. Fukumura DAI, Jain RK. Imaging angiogenesis and the microenvironment. APMIS. 2008; 116:695–715. [PubMed: 18834413]
33. Hu S, Wang LV. Photoacoustic imaging and characterization of the microvasculature. J Biomed Opt. 2010; 15:011101. [PubMed: 20210427]
34. Vakoc BJ, Lanning RM, Tyrrell JA, Padera TP, Bartlett LA, et al. Three-dimensional microscopy of the tumor microenvironment in vivo using optical frequency domain imaging. Nat Med. 2009; 15:1219–1223. [PubMed: 19749772]
35. Cho CH, Sung HK, Kim KT, Cheon HG, Oh GT, et al. COMP-angiopoietin-1 promotes wound healing through enhanced angiogenesis, lymphangiogenesis, and blood flow in a diabetic mouse model. Proc Natl Acad Sci USA. 2006; 103:4946–4951. [PubMed: 16543381]
36. Ambrozy E, Waczulikova I, Willfort-Ehringer A, Ehringer H, Koppensteiner R, et al. Microcirculation in mixed arterial/ venous ulcers and the surrounding skin: clinical study using a laser Doppler perfusion imager and capillary microscopy. Wound Repair Regen. 2009; 17:19–24. [PubMed: 19152647]
37. Dunn AK, Devor A, Bolay H, Andermann ML, Moskowitz MA, et al. Simultaneous imaging of total cerebral hemoglobin concentration, oxygenation, and blood flow during functional activation. Opt Lett. 2003; 28:28–30. [PubMed: 12656525]
38. Werner S, Grose R. Regulation of wound healing by growth factors and cytokines. Physiol Rev. 2003; 83:835–870. [PubMed: 12843410]
39. Eming SA, Brachvogel B, Odorisio T, Koch M. Regulation of angiogenesis: wound healing as a model. Prog Histochem Cytochem. 2007; 42:115–170. [PubMed: 17980716]
40. Roesken F, Uhl E, Curri SB, Menger MD, Messmer K. Acceleration of wound healing by topical drug delivery via liposomes. Langenbecks Arch Surg. 2000; 385:42–49. [PubMed: 10664120]
41. Vollmar B, El-Gibaly AM, Scheuer C, Strik MW, Bruch HP, et al. Acceleration of cutaneous wound healing by transient p53 inhibition. Lab Invest. 2002; 82:1063–1071. [PubMed: 12177245]
42. Schafer M, Werner S. Cancer as an overhealing wound: an old hypothesis revisited. Natl Rev Mol Cell Biol. 2008; 9:628–638.
43. Nagy JA, Chang SH, Shih SC, Dvorak AM, Dvorak HF. Heterogeneity of the tumor vasculature. Semin Thromb Hemost. 2010; 36:321–331. [PubMed: 20490982]
44. Escamez MJ, Garcia M, Larcher F, Meana A, Munoz E, et al. An in vivo model of wound healing in genetically modified skin-humanized mice. J Invest Dermatol. 2004; 123:1182–1191. [PubMed: 15610532]
45. Apikoglu-Rabus S, Izzettin FV, Turan P, Ercan F. Effect of topical insulin on cutaneous wound healing in rats with or without acute diabetes. Clin Exp Dermatol. 2009; 35:180–185. [PubMed: 19594766]
46. Tian J, Wong KKY, Ho C-M, Lok C-N, Yu W-Y, et al. Topical delivery of silver nanoparticles promotes wound healing. Chem Med Chem. 2007; 2:129–136. [PubMed: 17075952]
47. Bao P, Kodra A, Tomic-Canic M, Golinko MS, Ehrlich HP, et al. The role of vascular endothelial growth factor in wound healing. J Surg Res. 2009; 153:347–358. [PubMed: 19027922]
48. Wu Y, Chen L, Scott PG, Tredget EE. Mesenchymal stem cells enhance wound healing through differentiation and angiogenesis. Stem Cells. 2007; 25:2648–2659. [PubMed: 17615264]

Author Manuscript

Author Manuscript

Author Manuscript

Author Manuscript

49. Dvorak HF. Tumors: wounds that do not heal. Similarities between tumor stroma generation and wound healing. N Engl J Med. 1986; 315:1650–1659. [PubMed: 3537791]
50. Jain RK. Normalization of tumor vasculature: an emerging concept in antiangiogenic therapy. Science. 2005; 307:58–62. [PubMed: 15637262]
51. Dewhirst MW, Richardson R, Cardenas-Navia I, Cao Y. The relationship between the tumor physiologic microenvironment and angiogenesis. Hematol Oncol Clin N Am. 2004; 18:973–990.
52. Bullitt E, Zeng D, Gerig G, Aylward S, Joshi S, et al. Vessel tortuosity and brain tumor malignancy: a blinded study1. Acad Radiol. 2005; 12:1232–1240. [PubMed: 16179200]

Author Manuscript

Author Manuscript

Author Manuscript

Author Manuscript

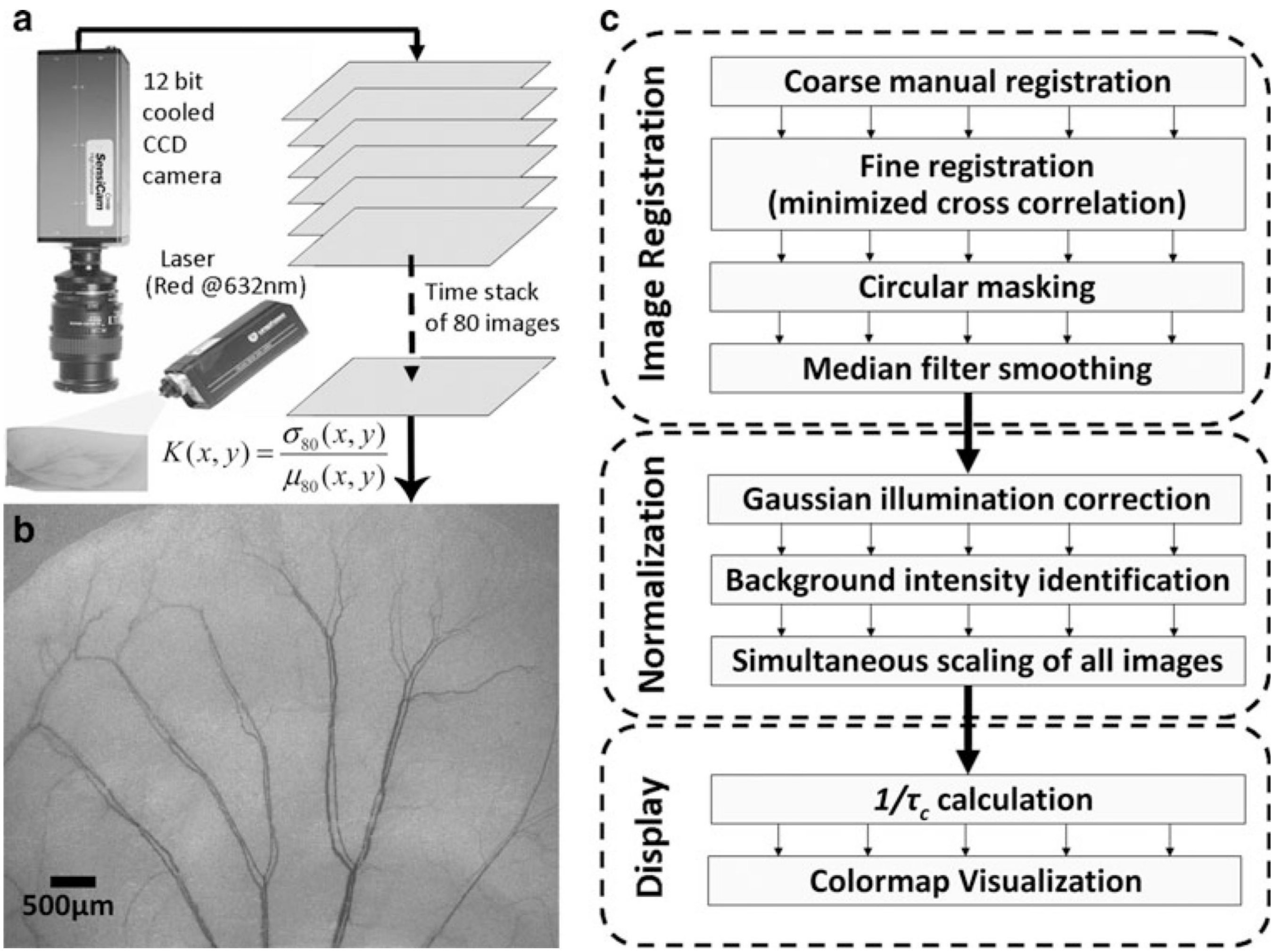

Fig. 1.

LSCI technique for longitudinal imaging of mouse ear vasculature: **a** LSCI consists of acquisition of a time stack of 80 images of the immobilized mouse ear using a 12 bit cooled CCD camera and its subsequent processing using the temporal speckle contrast equation to obtain a high resolution and high contrast, yet wide field image of the mouse ear vasculature. **b** An example image of the mouse ear vasculature obtained using LSCI. Note that the field of view is 6.4 mm × 4.8 mm with the smallest vessel visible having a diameter of 20 µm (3 pixels). **c** The post-processing steps required to monitor angiogenic response over the course of multiple imaging sessions through the wound healing period. Each image is first registered to the baseline and the intensity values are normalized to compare flow over multiple images. Finally, the images are color-coded for improved visualization of tissue blood flow

Author Manuscript

Author Manuscript

Author Manuscript

Author Manuscript

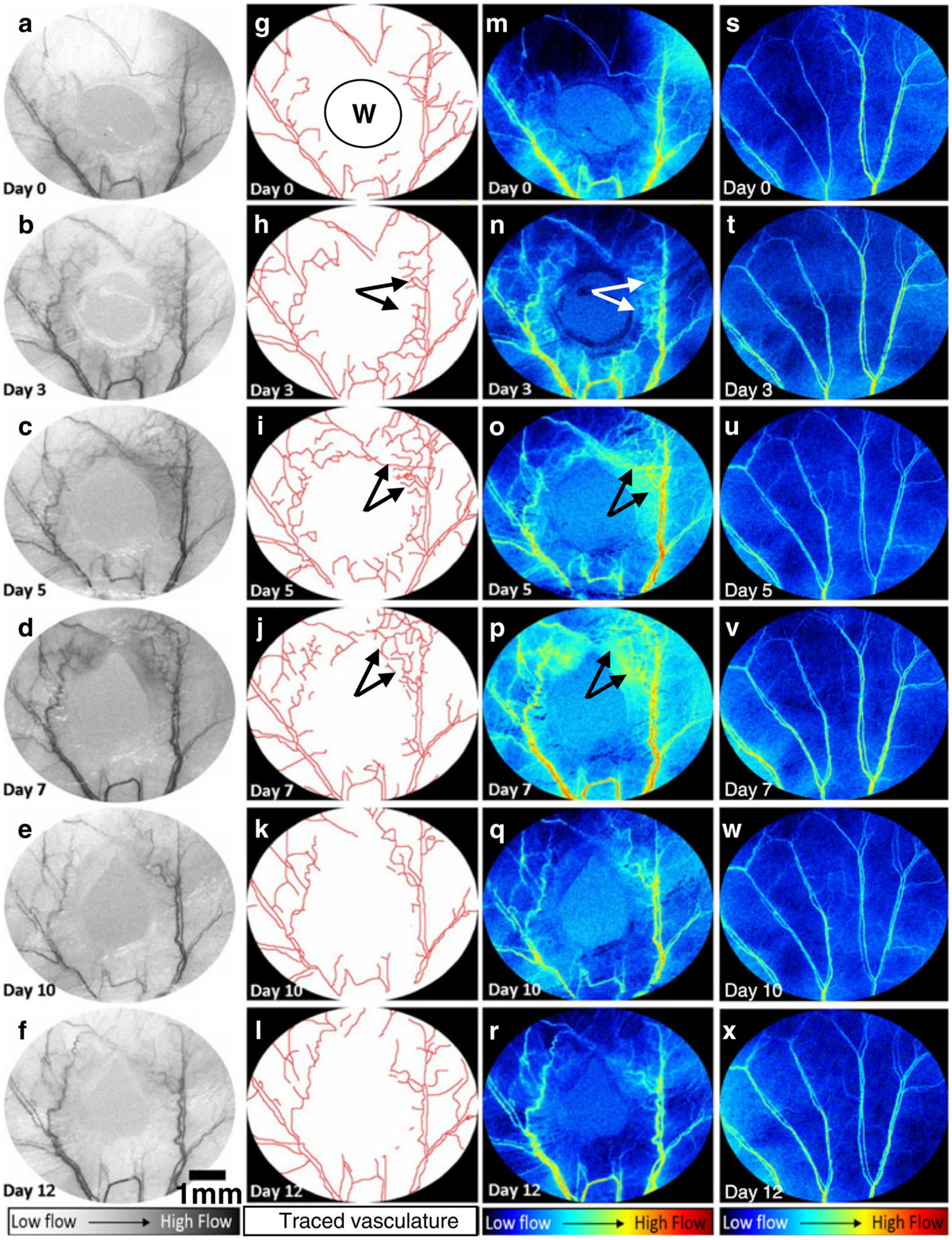

Fig. 2.

In vivo angiogenic response during wound healing using LSCI in a mouse ear model: The *first column* (**a–f**) shows representative sequential LSCI images acquired on days 0, 3, 5, 7, 10 and 12 after wound creation (indicated by W). The outlines of these vessels were manually segmented as shown in *the second column* (**g–l**). The *third column* (**m–r**) shows the changes in blood flow ($1/\tau_c$ values) that occur during the wound healing period. For comparison, the *fourth column* (**s–x**) shows changes in blood flow ($1/\tau_c$ values) over the same period in a control mouse ear. These color mapped images were obtained using the procedure described in Fig. 1c. Regions indicated by *arrows* exhibited an increase in neovascularization and average flow until day 7, which then subsided as healing completed

Author Manuscript Author Manuscript Author Manuscript Author Manuscript

Author Manuscript Author Manuscript Author Manuscript Author Manuscript

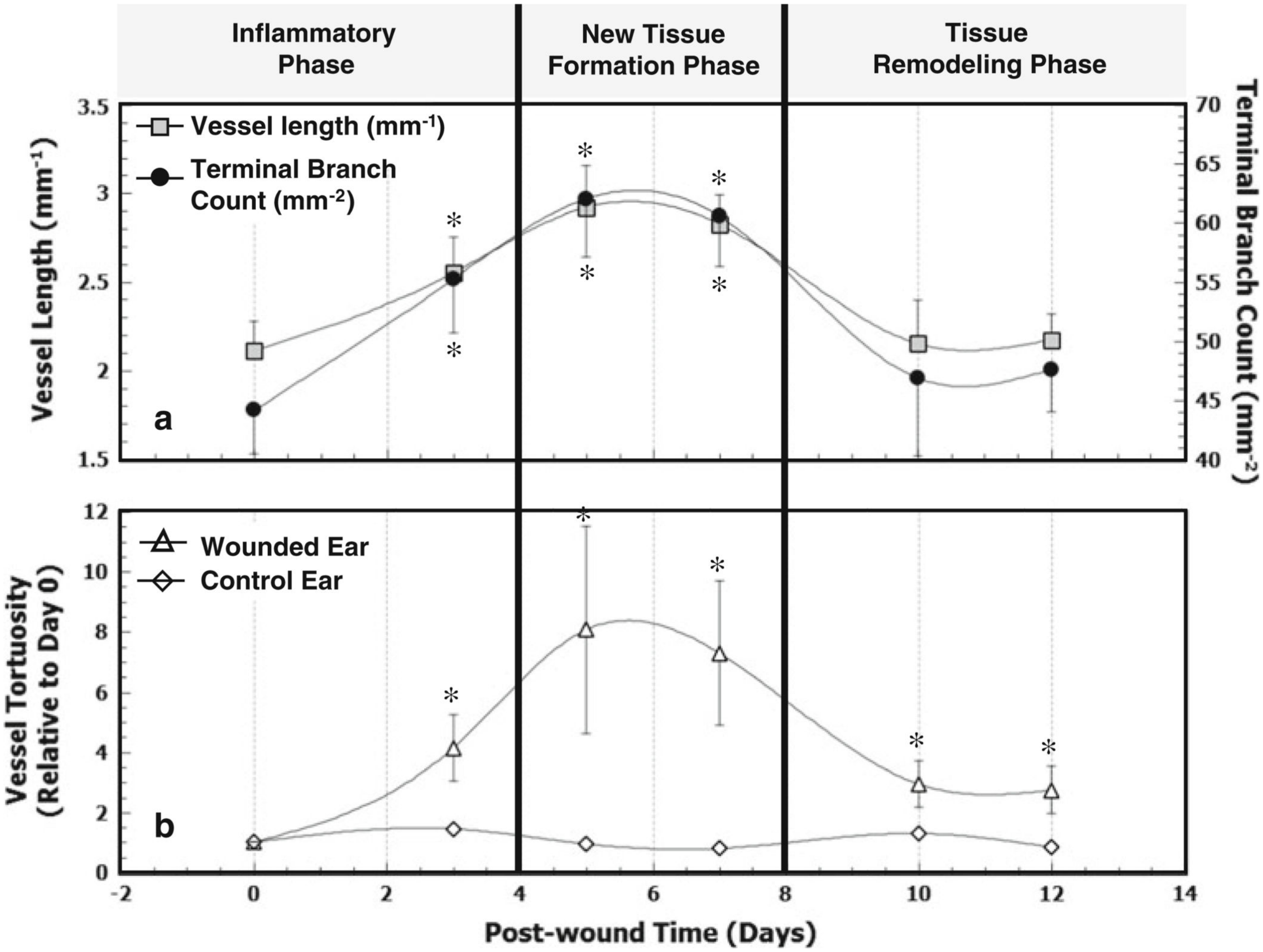

Fig. 3.

In vivo changes in vascular morphology during wound healing: The vascular response was monitored using LSCI on days 0, 3, 5, 7, 10 and 12 after wound creation. Blood vessels were manually traced and both, vessel length as well as the number of terminal vessel branches were counted to quantify the degree of neovascularization. **a** Longitudinal trends in vessel length and TB count calculated per unit area (mm^2) of healing skin in the wound periphery. *Asterisks* indicate that vessel lengths and terminal branch counts for days 3, 5, and 7 were significantly different from those on day 0. **b** Changes in tortuosity of parent feeding blood vessel during wound healing. The *plot* shows the mean tortuosity over the 12 day course of wound healing. The tortuosity of the unwounded controls did not vary significantly. *Asterisks* indicate that vessel tortuosity in the wounded ear was significantly greater than that in the control ear on days 3 ($P = 0.02$), 5 ($P = 0.05$), 7 ($P = 0.03$), 10 ($P = 0.08$) and 12 ($P = 0.06$)

Author Manuscript

Author Manuscript

Author Manuscript

Author Manuscript

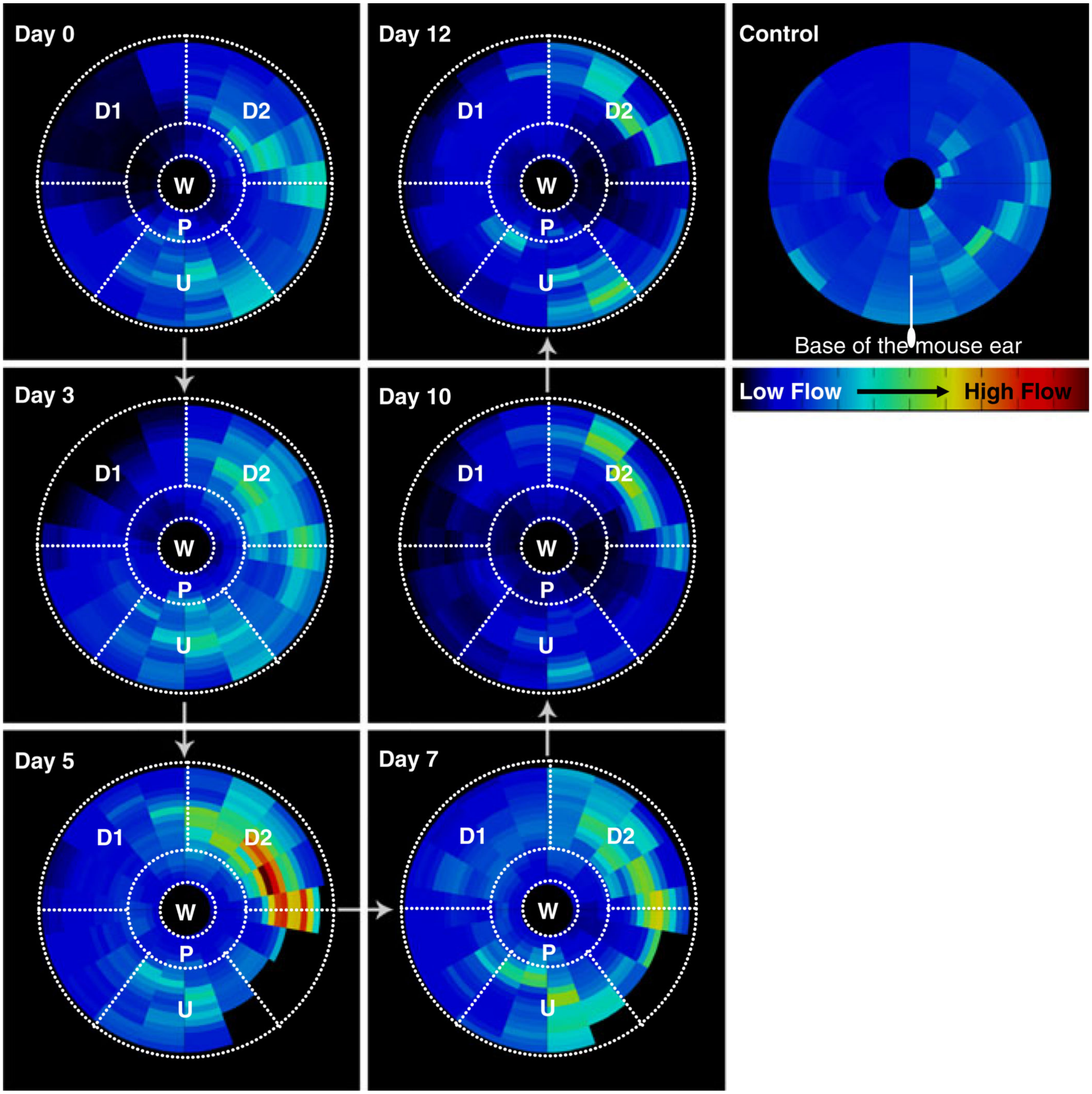

Fig. 4.

Spatiotemporal analysis of in vivo blood flow changes in the wound periphery: This *circular plot* illustrates the mean blood flow (computed from all mice in the cohort) in the wound periphery as a function of its orientation with respect to the wound and the base of the ear. The wound is represented on all *plots* as a *circle* of fixed diameter and *each concentric region* around it represents a 50 μm wide region. The radial distance on *each plot* is the shortest distance of that region from the wound outline, and is analyzed in increments of 50 μm. Similarly, the angle (0° < θ < 360°) on the *plots* is the angle that a line joining the region with the wound center subtends with the line joining the base of the ear with wound center in the counter clockwise direction. Salient observations were made in each of the following ROIs—W: wound, P: proximal region, U: upstream region, D1: downstream region 1, D2: downstream region 2

Author Manuscript Author Manuscript Author Manuscript Author Manuscript

Author Manuscript
Author Manuscript
Author Manuscript
Author Manuscript

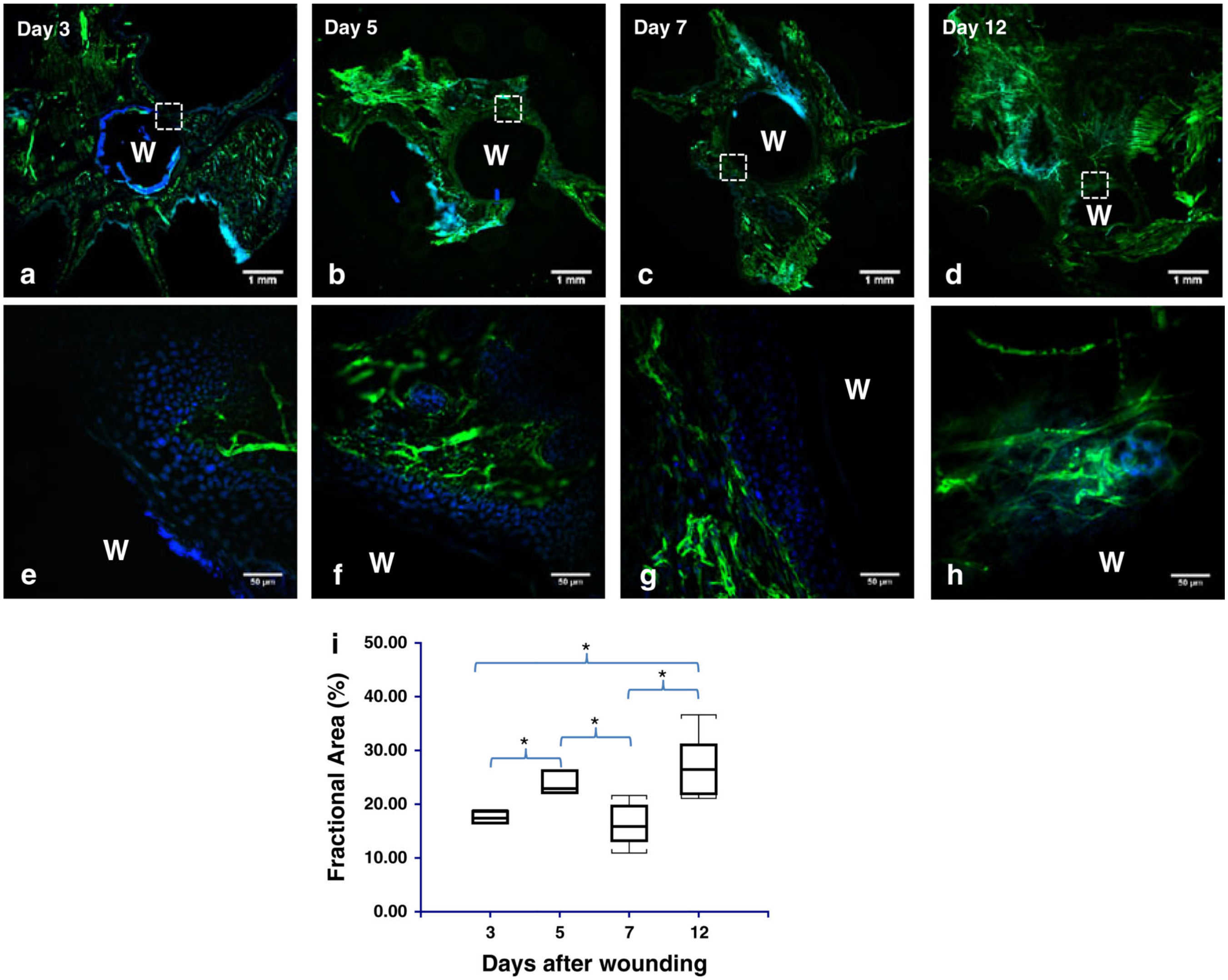

Fig. 5.

Histological validation of vascular remodeling during wound healing: **a–d** Representative low magnification (2×) images of sections from the flattened mouse ear pinna in which the blood vessel endothelia are labeled with laminin (*green*) and nuclei with DAPI (*blue*). The wound is indicated by 'W' in all *panels*. **e–g** High magnification (40×) images of the region indicated by the hatched square in (**a–d**). The wound granulation layer starts out as avascular (**e**), obtains some peripheral vascularization (**f**), followed by additional peripheral vascularization (**g**), and finally becomes well vascularized (**h**). **i** *Box* and *whisker plot* of the fractional area of laminin staining at days 3, 5, 7 and 12. The fractional area was a significantly elevated at days 5 and 7 relative to day 3 and at days 5 and 12 relative to day 7